

To appear in the 2005 Sep issue of the *Astronomical Journal*.

Faint Radio Sources in the NOAO Boötes Field. VLBA Imaging and Optical Identifications

J. M. Wrobel,¹ G. B. Taylor,^{1,2} T. A. Rector,^{1,3} S. T. Myers,¹ and C. D. Fassnacht⁴

ABSTRACT

As a step toward investigating the parsec-scale properties of faint extragalactic radio sources, the Very Long Baseline Array (VLBA) was used at 5.0 GHz to obtain phase-referenced images of 76 sources in the NOAO Boötes field. These 76 sources were selected from the FIRST catalog to have peak flux densities above 10 mJy at 5" resolution and deconvolved major diameters of less than 3" at 1.4 GHz. Fifty-seven of these faint radio sources were identified with accretion-powered radio galaxies and quasars brighter than 25.5 mag in the optical *I* band. On VLA scales at 1.4 GHz, a measure of the compactness of the faint sources (the ratio of the peak flux density from FIRST to the integrated flux density from the NVSS catalog) spans the full range of possibilities arising from source-resolution effects. Thirty of the faint radio sources, or $39^{+9}_{-7}\%$, were detected with the VLBA at 5.0 GHz with peak flux densities above $6\sigma \sim 2$ mJy at 2 mas resolution. The VLBA detections occur through the full range of compactness ratios. The stronger VLBA detections can themselves serve as phase-reference calibrators, boding well for opening up much of the radio sky to VLBA imaging. For the adopted cosmology, the VLBA resolution corresponds to 17 pc or finer. Most VLBA detections are unresolved or slightly resolved but one is diffuse and five show either double or core-jet structures; the properties of these latter six are discussed in detail. Three VLBA detections are unidentified and fainter than 25.5 mag in the optical *I* band; their properties are highlighted because they likely mark optically-obsured active nuclei at high redshift.

¹National Radio Astronomy Observatory, P.O. Box O, Socorro, NM 87801; jwrobel@nrao.edu, gaylor@nrao.edu, smyers@nrao.edu

²Kavli Institute of Particle Astrophysics and Cosmology, Menlo Park, CA 94025

³Physics & Astronomy Department, University of Alaska Anchorage, 3211 Providence Drive, Anchorage, AK 99508; aftar@uaa.alaska.edu

⁴Department of Physics, University of California at Davis, 1 Shields Avenue, Davis, CA 95616; cdfassnacht@ucdavis.edu

Subject headings: astrometry — galaxies: active — radio continuum — surveys

1. Introduction

During the past decade, over two thousand radio continuum sources have been surveyed at milliarcsecond (mas) resolution with the techniques of very long baseline interferometry (VLBI; e.g. Beasley et al. 2002; Fomalont et al. 2003; Petrov et al. 2005). Optical identifications and redshifts are time-consuming to obtain and are available only for a few hundred sources (Vermeulen et al. 2003; Kellermann et al. 2004). For those sources, the accepted paradigm is that VLBI imaging traces the relativistic outflows on parsec scales that emerge from the accretion regions of supermassive black holes. These traditional surveys rely on self-calibration techniques and are therefore biased by targeting sources brighter than about 50 mJy (e.g. Taylor et al. 2005). Moreover, these surveys only target sources with flat radio spectra, to enhance the prospects that synchrotron-self-absorbed emission will be present on mas scales. Do the parsec-scale properties of the fainter radio population, selected independent of radio spectra, differ from the properties inferred for the brighter, flat-spectrum population?

Addressing this question is now feasible because of three recent developments. First, the technique of phase referencing is now in routine use on VLBI arrays (Wrobel et al. 2000),¹ enabling astrometric imaging of sources fainter than 50 mJy (e.g., Xu et al. 2000). Second, wide-area radio surveys with sub-arcminute resolution have defined source populations at millijansky levels (e.g., Condon 1999). Third, the prior difficulties with obtaining optical identifications and redshifts can be mitigated by focusing on faint radio sources within known optical deep fields (e.g., Cristiani et al. 2001). Combining these three developments, the NRAO Very Long Baseline Array² (VLBA; Napier et al. 1994) was used to conduct phase-referenced observations at 5.0 GHz of faint radio sources in the 9 deg² of the NOAO Boötes field (Jannuzi & Dey 1999; Jannuzi et al. 2005; Dey et al. 2005). The NOAO limit of $I \sim 25.5$ (Vega) mag means it is feasible that many of these faint sources can be identified, dominantly with accretion-powered radio galaxies and quasars (Jannuzi & Dey 1999), and efficient follow-up with a multi-object fiber spectrograph is possible. The idea for this type of VLBI survey was first suggested by Garrett & Garrington (1998). Giovannini et al. (2005) are pursuing a different strategy that will, eventually, include some sources too faint for

¹ Available at <http://www.vlba.nrao.edu/memos/sci/sci24memo.ps>.

²The VLBA is operated by the National Radio Astronomy Observatory, a facility of the National Science Foundation, operated under cooperative agreement by Associated Universities, Inc.

VLBI self-calibration; that survey is targeting a complete sample of 95 radio sources selected independently of the presence of compact emission and at redshifts $z < 0.1$. Also, Porcas et al. (2004) have been using a single VLBI baseline (Arecibo-Effelsberg) to perform a survey of approximately 1000 radio sources, independent of source flux density, size or spectrum.

This paper is organized as follows. Section 2 describes the sample selection for the VLBA survey, including the identification status in the I band available from Jannuzzi et al. (2005). The VLBA observations and calibration are described in Section 3, while Section 4 describes the VLBA imaging strategies. The discussion begins with an overview of the VLBA survey (Section 5.1) then explores implications related to the VLBA detection rate (Section 5.2), the VLBA parsec-scale structures (Section 5.3), and the characteristics of the eight VLBA detections unidentified in the NOAO Boötes survey (Section 5.4). Section 6 closes with a summary of this paper and also outlines future steps concerning this sample of faint radio sources (Rector et al. 2005, in preparation).

To facilitate comparison with other analyses in the NOAO Boötes field (Eisenhardt et al. 2004; Houck et al. 2005; Higdon et al. 2005), this paper will use Vega magnitudes and a flat Λ CDM cosmology with $H_0 = 71 \text{ km s}^{-1} \text{ Mpc}^{-1}$, $\Omega_m = 0.27$, and $\Omega_\Lambda = 0.73$ (Spergel et al. 2003). Also, all quoted uncertainties will correspond to 1σ Gaussian errors, including those for Poisson counting errors as tabulated by Gehrels (1986).

2. Sample Selection

The faint radio sources were selected from the 1999 July 21 version of the FIRST catalog (Faint Images of the Radio Sky at Twenty-Centimeters; White et al. 1997) to have peak flux densities above 10 mJy at $5''$ resolution and deconvolved major diameters of less than $3''$ at 1.4 GHz. Figure 1 shows the locations of these 76 faint and compact sources, while Table 1 lists for each source the position-encoded FIRST name in column 1 and the peak flux density from FIRST at 1.4 GHz in column 2. Column 3 gives the integrated flux density at 1.4 GHz obtained from the 2002 July 18 version of the NVSS catalog at $45''$ resolution (NRAO VLA Sky Survey; Condon et al. 1998). Each FIRST source has a localization ellipse diameter at 5σ of about $1.0''$, so it is prudent to ensure that the VLBA search region covers a diameter of at least $1.0''$.

A cross-correlation of the 76 FIRST sources with the NOAO I band catalog (Jannuzzi et al. 2005) was made. Only identifications within a total offset of $3''$ were considered as potential matches, although none were found with offsets between $2\text{-}3''$. Rector et al. (2005, in preparation) will discuss these NOAO identifications in detail. For now, we note only that

55 of these faint radio sources have been identified with accretion-powered radio galaxies and quasars. Column 4 of Table 1 indicates the identification status in the *I* band of the FIRST sources.

On VLA scales at 1.4 GHz, the ratio of the peak flux density from FIRST (column 2, Table 1) to the integrated flux density from the NVSS (column 3, Table 1) is a measure of the compactness of the FIRST sources. This compactness ratio is plotted in Figure 2 as a function of the NVSS flux density, with plot symbols encoding the identification status for the FIRST sources (column 4, Table 1). The FIRST and NVSS observations occurred in 1994 July and 1995 April, respectively. In the absence of source variability, all sources are expected to be located within the region defined by the dashed lines. Figure 2 shows that the compactness ratios span the full range of possibilities arising from source-resolution effects (from zero to unity), while the few instances of ratios significantly exceeding unity could plausibly be attributed to source variability. Figure 2 also shows that the unidentified sources are spread throughout a wide range of compactness ratios.

3. VLBA Observations and Calibration

The VLBA was used to observe the 76 FIRST sources and calibrators during four observing segments described in Table 2. For each segment, antenna separations spanned 240 km to 8600 km. Data were acquired during about 6.5 hours in dual circular polarizations with 4-level sampling and at a center frequency 4.97949 GHz with a bandwidth of 32 MHz per polarization. This bandwidth was synthesized from 4 contiguous baseband channels, each of width 8 MHz. A strong calibrator 3C 279 was observed to align the phases of the independent baseband channels. Observation and correlation assumed a coordinate equinox of 2000. Correlation also assumed an integration time of 2 seconds, 32 spectral points per baseband channel, and a single pass at the *a priori* position of each FIRST source. While there were a few instances where several FIRST sources fell within the primary beam of a VLBA antenna, correlation was done only for the FIRST source at the peak of the primary beam.

Phase-referenced observations were made in the nodding style at elevations above 20°. Successive 80-second observations of three FIRST sources were preceded and followed by a 60-second observation of the phase, rate, and delay calibrator (referred to as a phase calibrator hereafter) listed in Table 2, leading to a switching time of 5 minutes. *A priori* positions for the phase calibrators were available in the International Celestial Reference Frame (Extension 1) (ICRF-Ext.1; IERS 1999; Ma et al. 1998), so all FIRST sources detected with the VLBA will have their positions measured in that frame. Each FIRST source was

observed during six snapshots spread over time to enhance coverage in the (u, v) plane. For each segment, a maximum switching angle of 2.5° was used to assign FIRST sources to the segment’s phase calibrator. As is evident from Figure 1, this procedure failed for one source (FIRST J143152.544+340110.15), for which a maximum switching angle of 2.6° was required. Two phase calibrators were used during segment 3 to reach different FIRST sources, so that segment is conceptually split into segments 3a and 3b depending on which phase calibrator was used (Table 2). To help assess repeatability, some FIRST sources were observed during two segments. An observing frequency of 5.0 GHz was used to optimize the chances that phase-referencing would succeed for all switching angles; phase-referencing at lower (higher) frequencies can be harmed by ionospheric (tropospheric) effects (Wrobel et al. 2000).

Figure 1 and Table 2 also identify check calibrators that were observed similarly to each FIRST source but with the switching angles indicated. Those calibrator observations were intended to serve two purposes. First, the tabulated positions are accurate to better than 1.3 mas per coordinate in the ICRF-Ext.1 and can be used to check the differential astrometry. Second, the calibrator data can be used to check the coherence losses. Phase calibrators for some segments served as check calibrators for other segments. Check calibrators J1416+3444, F14543631, and F14653289 were also taken from the table’s references. The latter two check calibrators were originally selected from Myers et al. (2003) to improve upon the calibrator density offered in Beasley et al. (2002).

For each segment, data editing and calibration were done with the NRAO AIPS software and following the strategies outlined in Appendix C of the NRAO AIPS Cookbook³. Data deletion was based on system flags recorded at observation and tape weights recorded at correlation. Corrections for the dispersive delays caused by the Earth’s ionosphere were made using electron-content models based on Global Positioning System data and derived at the Jet Propulsion Laboratory. VLBA system temperatures and gains were used to set the amplitude scale to an accuracy of about 5%, after first correcting for sampler errors. The visibility data for the phase calibrator were used to generate phase-referenced visibility data for the appropriate check calibrators (Table 2) and for the subset of FIRST sources observed during that segment (Table 1). In contrast, the visibility data for the phase calibrator and the strong calibrator 3C 279 were self-calibrated.

Parallel and cross-hand correlations were obtained for each segment. A polarization calibration was done for the first segment, but each FIRST source was so faint in Stokes I that Stokes Q and U were emission-free and did not usefully constrain the linear polarization

³<http://www.aoc.nrao.edu/aips/cook.html>

percentage $100\sqrt{Q^2 + U^2}/I$. Thus for later segments a polarization calibration was not attempted. For all segments, however, the emission-free information in Stokes Q for each FIRST source proved to be a useful cross-check of the detection threshold adopted in Stokes I .

4. VLBA Imaging Strategies

The AIPS task IMAGR was used to image the Stokes I and Q emission from each FIRST source and each calibrator. To reduce side-lobe levels for these VLBA multi-snapshot data, the visibility data were weighted uniformly with robustness 0.5 and a sensitivity loss of about 10% relative to natural weighting was incurred. A two-stage approach to the imaging was taken.

The first image, not cleaned, spanned 4096×0.35 mas in each coordinate and had a typical angular resolution characterized as an elliptical Gaussian with FWHM dimensions of 3.0 mas by 1.5 mas aligned nearly north-south (referred to as a resolution of 2 mas hereafter). This image is within the field-of-view limits set by time and bandwidth averaging (Wrobel 1995); the most constraining limit follows from accepting, at the field edge, a 10% drop in the peak amplitude due to averaging over each 8-MHz baseband channel, resulting in an elliptical field of view aligned nearly north-south with major and minor axes of 3000 mas and 1500 mas, respectively. A search σ was obtained by forming a histogram of brightness variations from pixel to pixel within the search region and evaluating the root-mean-square of that histogram. Given the array, observation, and imaging parameters, a detection threshold of $6\sigma \sim 2$ mJy was adopted within the search region, a square of side 1400 mas. Values for the search σ vary from image to image and appear in column 6 of Table 1. For Stokes I , the right ascension and declination of the peak of that detection was recorded. For Stokes Q , the emission-free search region was analysed to cross-check and validate the 6σ detection threshold for Stokes I . For a strong Stokes I detection, the quoted value for the search σ is typically higher than expected from thermal sensitivity, because the histogram for the search region is corrupted by side-lobes from the strong detection (the high-valued pixels of a strong Stokes I detection were excluded from the histogram). Analysis of this first set of images resulted in VLBA detections of 30 of the FIRST sources in Table 1 and all calibrators.

A second image of Stokes I was made for each VLBA detection, including the 30 faint sources and all calibrators. This second image spanned 512×0.35 mas in each coordinate and was made by shifting the tangent point, as derived from the right ascension and declination of the peak in the first image, to the field center. These shifted images were cleaned in regions centered on the detections and spanning 2.1 mas east-west and 3.5 mas north-south for the

isolated detections but spanning customized regions for the extended detections. These shifts were finite for the phase-referenced and cleaned images shown in Figures 3-5 but zero by definition for the self-calibrated and cleaned images of the phase and strong calibrators.

4.1. Residual Phase Errors and VLBA Nondetections

Residual errors during phase referencing will degrade the point-source sensitivity of the VLBA. To quantify the effect of this loss of coherence, individual 80-second observations of the check calibrators listed in Table 2 were phase self-calibrated, imaged, and cleaned. The ratios of the peak intensities in the self-calibrated images were 1.0 to 1.4 times the peak intensities in the phase-referenced images, as tabulated in column 10 of Table 2. Observations of these calibrators required switching angles of 0.6 to 2.7°, but switching angles of 2.6° or less were needed to reach the FIRST sources. While there may be some segment-to-segment variations, a conservative correction for the loss of point-source sensitivity is about 1.2. For the VLBA nondetections in Table 1, the quoted 6σ upper limits for a point source have been increased by this factor.

4.2. Modelfitting the VLBA Detections

The bright components in the phase-referenced images (Figs. 3-5) appear to be slightly resolved, but this apparent resolution is probably mostly artificial and due to the residual phase errors discussed in subsection 4.1. In most cases, a single elliptical Gaussian was fit to each of these VLBA images to yield the position peak and integrated flux densities quoted in Table 1. For a few images, two elliptical Gaussians were fit and their integrated flux densities were summed and tabulated along with the position of the brighter Gaussian. For the source showing very diffuse structure, areal integration yielded the tabulated integrated flux density and a parabolic fit of the brightest structure yielded the tabulated position. A few sources were too weak for reliable Gaussian fitting; each of them is considered as a provisional VLBA detection, with a parabolic fit yielding the tabulated peak flux density (corrected for coherence losses) and position.

For the VLBA integrated flux density, no corrections were made for coherence losses and the tabulated error is the quadratic sum of the 5% scale error and the error in the Gaussian model. Although the phase errors leading to coherence loss do broaden the VLBA detections, coherence corrections were not made because the flux densities can be largely recovered with Gaussian fitting. For the VLBA positions, the calculated error per coordinate is the quadratic

sum of three terms: (a) the 1σ error in the phase calibrator position; (b) the 1σ error in the differential astrometry; and (c) the 1σ error in the Gaussian fit. As indicated in the note to Table 2, term (a) is always less than 1 mas in one dimension; to be conservative, 1 mas is adopted for term (a). To quantify term (b), the positions of the check calibrators in Table 2 were measured in the phase-referenced images and subtracted from their *a priori* positions, leading to the position corrections, in right ascension and declination, tabulated in column 11 of Table 2. Observations of these check calibrators required switching angles of 0.6 to 2.7° , but switching angles of 2.6° or less were needed to reach the FIRST sources. While there may be some segment-to-segment variations, a conservative estimate for term (b) is 2 mas in one dimension. For the weakest VLBA detections of FIRST sources, term (c) has a worst-case value of 0.3 mas in the north-south direction and half that in the east-west direction; to be conservative, 1 mas is adopted for term (c). Thus for all the VLBA detections reported in Table 2, a conservative estimate of the position error per coordinate is the quadratic sum of 1 mas, 2 mas, and 1 mas, or 2.5 mas.

5. Discussion

5.1. VLBA Overview

Seventy-six faint radio sources were selected from the FIRST catalog to have peak flux densities above 10 mJy at $5''$ resolution and deconvolved major diameters of less than $3''$ at 1.4 GHz. The compactness ratio on VLA scales at 1.4 GHz, as defined in Section 3, is plotted in Figure 6 as a function of the VLBA photometry at 5.0 GHz (column 9, Table 1). As for Figure 2, the plot symbols encode the identification status for the FIRST sources (column 5, Table 1). Figure 6 shows that VLBA detections occur over the full range of compactness ratios.

5.2. VLBA Detection Rate

Thirty of the 76 FIRST sources, or $39^{+9\%}_{-7\%}$, were detected with the VLBA at 5.0 GHz with peak flux densities above $6\sigma \sim 2$ mJy at 2 mas resolution. For 20 similar but somewhat fainter sources in the *Spitzer* First-Look Survey (Condon et al. 2003), twelve sources, or $60^{+23\%}_{-17\%}$, were detected with the VLBA at 1.4 GHz, with peak flux densities above 2 mJy at 9 mas resolution (Wrobel et al. 2004). Equally good success rates can be expected when VLBA phase-referencing in the nodding style is used to target similar FIRST sources anywhere in that survey’s 10,000 deg 2 . Moreover, among the VLBA detections reported in Table 1,

FIRST J142910.223+352946.86 was used successfully as an in-beam phase calibrator (Wrobel et al. 2000) at 1.4 GHz for a VLBI survey of tens of sources covering 0.28 deg^2 in the NOAO Boötes Field (Garrett et al. 2005). This illustrates how the stronger VLBA detections can, themselves, serve as VLBI phase calibrators, potentially opening up much of the radio sky to phase-referencing in either the nodding or the in-beam styles.

5.3. VLBA Parsec-Scale Structures

For the adopted cosmology, the achieved VLBA resolution of 2 mas corresponds to 17 pc or finer, while each of the panels in Figures 3-5 spans 170 pc or less. Most VLBA detections at 5.0 GHz are unresolved or appear to be slightly resolved, with rest-frame brightness temperatures in the range $(2 - 50)(1 + z) \times 10^7 \text{ K}$, or more if truly unresolved. Such high brightness temperatures, in combination with the optical identifications discussed below, imply that these VLBA detections mark accretion-driven outflows on parsec scales. Also, one VLBA detection (FIRST J142905.105+342641.06) appears quite diffuse and elongated, as discussed in the appendix. Five others (FIRST J143121.320+332808.95, FIRST J143152.544+340110.15, FIRST J143449.111+354246.98, FIRST J143752.050+351940.08, and FIRST J143841.949+335809.48) show either double or core-jet structures, as mentioned in the appendix. The structures of these six VLBA detections further enforce an outflow scenario, and we now consider some issues that can be addressed based on these structures.

Could some of the five VLBA detections showing double or core-jet structures eventually yield evidence for counterjets, important for strong tests of unified schemes (Xu et al. 2000)? For sources selected independent of their radio spectra, more counterjets can be expected adjacent to core-jet structures, but may elude discovery until follow-up VLBA observations with higher sensitivity.

Might some of the five VLBA detections showing double or core-jet structures be compact symmetric objects (CSOs), young systems offering insights into evolutionary models for radio galaxies and strong tests of unified schemes (Taylor et al. 2000)? From VLBI imaging of a bright and flat-spectrum sample (Taylor et al. 1996), Taylor et al. (2000) note that about 7% show CSO structures. Using this as a rough guide for faint sources selected independent of their radio spectra, two CSO candidates can be expected among the 30 VLBA detections. But for sources selected independent of their radio spectra, more symmetric core-jet structures are to be expected, giving them the appearance of CSOs in the discovery images. Thus follow-up VLBA observations at other frequencies will be required to distinguish between candidate core-jets and candidate CSOs.

Finally, is it likely that some of the five VLBA detections showing double or core-jet structures could be gravitational millilenses, caused by a cosmic population of supermassive black holes (Wilkinson et al. 2001)? From VLBI imaging of a bright and flat-spectrum sample (Taylor et al. 1996), Wilkinson et al. (2001) find that for image separations 1.5–50 mas, the upper limit at 95%-confidence to the expected millilensing rate is about one lens per 430 sources. Using this as a rough guide for faint sources selected independent of their radio spectra, then two implications follow. First, the prospect of discovering one millilens candidate among 30 VLBA detections is slim. Second, expanding the present VLBA survey by a factor of 14 would lead to equally good constraints on the expected millilensing rate. More than a thousand sources would have been examined in the process, with about four in ten being VLBA detections searched for lensing signatures. This VLBA survey method uses 0.5 hours to observe three sources, so repeating the survey in 13 other regions would require additional observations totaling 164 hours.

5.4. VLBA Detections Unidentified in the NOAO Boötes Survey

Fifty-seven of the 70 FIRST sources, or 81%, were identified with accretion-powered radio galaxies and quasars using the NOAO data (Jannuzi et al. 2005). A similar identification percentage applies to the 27 VLBA detections, as 24, or 89%, were identified.

The three VLBA detections with fainter optical hosts must still mark active nuclei. One of these three is an apparent double with an 8-mas separation (FIRST J143121.320+332808.95), while the other two (FIRST J142738.625+330756.96 and FIRST J143643.209+352222.98) are unresolved or appear to be slightly resolved. These three unidentified VLBA detections at 5.0 GHz have rest-frame brightness temperatures in the range $(2 - 6)(1 + z) \times 10^7$ K, or more if truly unresolved. This is similar to the range of $(2 - 50)(1 + z) \times 10^7$ K for the identified VLBA detections that pin-point the active nuclei of the accretion-powered radio galaxies and quasars.

The three unidentified VLBA detections fainter than 25.5 mag in the *I* band are likely candidates for being optically-obsured active nuclei at high redshift. Also in the NOAO Boötes field, Garrett et al. (2005) recognized a similar case involving a VLBI detection at 1.4 GHz of an unidentified 20-mJy Westerbork source, while Higdon et al. (2005) report numerous cases of unidentified VLA sources in the mJy regime at 1.4 GHz, for which analysis of their spectral energy distributions (SEDs) supports an accretion-power origin. Rector et al. (2005, in preparation) will investigate the SEDs of the three unidentified VLBA detections mentioned above, paying particular attention to a comparison of their SEDs to those of the unidentified VLA sources analyzed by Higdon et al. (2005).

6. Summary and Future Steps

The VLBA was used at 5.0 GHz to obtain phase-referenced images of 76 sources in the NOAO Boötes field, selected from the FIRST catalog to have peak flux densities above 10 mJy at 5" resolution and deconvolved major diameters of less than 3" at 1.4 GHz. Fifty-seven of these faint radio sources were identified in the optical with accretion-powered radio galaxies and quasars with $I < 25.5$ mag. On VLA scales at 1.4 GHz, a measure of the compactness of the faint sources is the ratio of the peak flux density from FIRST to the integrated flux density from the NVSS catalog. These compactness ratios span the full range of possibilites arising from source-resolution effects. Also, the unidentified sources are spread throughout a wide range of compactness ratios.

Thirty of the faint radio sources ($39^{+9\%}_{-7\%}$) were detected with the VLBA at 5.0 GHz, with peak flux densities above $6\sigma \sim 2$ mJy at 2 mas resolution. The VLBA detections occur through the full range of compactness ratios. For the adopted cosmology, the VLBA resolution correponds to 17 pc or finer. Most VLBA detections are unresolved or slightly resolved. The resulting high brightness temperatures, in combination with the optical identifications, imply that these VLBA detections mark accretion-driven outflows on parsec scales. Moreover, the elongated structures of six VLBA detections further enforce an outflow scenario. Three VLBA detections are unidentified and fainter than 25.5 mag in the I band, similar to another VLBI detection reported by Garrett et al. (2005). These four VLBI detections are likely candidates for being optically-obsured active nuclei at high redshift, so understanding them is essential for completing the cosmic census of supermassive black holes.

For these faint radio sources in the NOAO Boötes field, the next steps involve obtaining redshifts, assessing intrinsic properties, examining the properties of the optical counterparts and their cluster environments, assembling the SEDs of the active nuclei, and tying data for the Boötes field to the ICRF. These topics will be covered by Rector et al. (2005, in preparation). Here we simply note that concerning the SEDs, for the 30 VLBA detections in Table 1, the photometry quantifies the emission from the active nuclei at 5.0 GHz; while for the 46 VLBA nondetections in Table 1, the photometry imposes upper limits on the emission from the active nuclei at 5.0 GHz. Rector et al. (2005, in preparation) will present further constraints on the SEDs of the active nuclei from the NOAO (Jannuzi et al. 2005; Dey et al. 2005) and *Spitzer* photometry (Eisenhardt et al. 2004; Houck et al. 2005). In Figure 1, the crosses in the north-east corner of the Boötes field show the four X-ray sources from Wang et al. (2004) with FIRST counterparts; unfortunately, all are weaker than the 10 mJy threshold adopted for this study. An X-ray survey covering more of the Boötes field is clearly needed. Finally, we note that concerning the ICRF, twenty-four of the VLBA detections are identified (column 5, Table 1, Fig. 6), so the VLBA astrometry will help anchor the multiwavelength

data for the NOAO Boötes field to the ICRF.

We acknowledge the anonymous referee for suggestions that helped clarify the manuscript and Ian McGreer for identification feedback. The calibrator source positions listed in Table 2 in the frame of the ICRF-Ext.1 catalog were provided by observations from the joint NASA/USNO/NRAO geodetic/astrometric program. This work made use of images and/or data products provided by the NOAO Deep Wide-Field Survey (Jannuzi & Dey 1999; Jannuzi et al. 2005; Dey et al. 2005), which is supported by the National Optical Astronomy Observatory (NOAO). NOAO is operated by AURA, Inc., under a cooperative agreement with the National Science Foundation.

A. Notes on Individual Sources

This appendix contains notes on the sources flagged in Table 1. An NVSS secondary is noted if present with an offset of less than $90''$. A FIRST secondary is noted if present within a square of side $90''$ centered on the FIRST position. A note appears for all VLBA detections.

FIRST J142456.287+352841.80: An NVSS secondary is also present, with $S_I = 16.7 \pm 0.6$ mJy offset by $68''$ at PA 83° . The FIRST image shows secondaries to the east and west of the FIRST position. The VLBA images in Fig. 3 from segments 1 and 2 have 1σ noise levels of 0.23 and 0.30 mJy beam $^{-1}$, respectively. Possibly a photometric variable at 5.0 GHz at 2 mas resolution. There is a counterpart in the optical I band so this VLBA detection will help link data for the Boötes field to the ICRF.

FIRST J142524.214+340935.68: The VLBA image in Fig. 3 has a 1σ noise level of 0.32 mJy beam $^{-1}$. There is a counterpart in the optical I band so this VLBA detection will help link data for the Boötes field to the ICRF.

FIRST J142607.716+340426.29: The VLBA image in Fig. 3 has a 1σ noise level of 0.34 mJy beam $^{-1}$. There is a counterpart in the optical I band so this VLBA detection will help link data for the Boötes field to the ICRF.

FIRST J142617.948+344039.63, FIRST J142623.374+343950.45: These FIRST sources are part of the same NVSS double. FIRST J142623.374+343950.45 is identified in the optical I band and appears isolated in the FIRST image. FIRST J142623.374+343950.45 is unidentified in the optical I band and shows a secondary in the north-west quadrant of the FIRST image; perhaps it is a lobe hotspot energized by the active nucleus in the optical host for FIRST J142623.374+343950.45.

FIRST J142659.719+341200.21: The FIRST source is the central component of an NVSS double with the tabulated S_I . The NVSS double shows Fanaroff-Riley I structure in the north-east and south-west quadrants of the FIRST image.

FIRST J142738.625+330756.96, FIRST J142739.694+330744.45: These FIRST sources are part of the same NVSS source, so they share the same tabulated S_I from NVSS. FIRST J142738.625+330756.96 is provisionally detected with the VLBA and is unidentified in the optical I band; its VLBA image shown in Fig. 3 has a 1σ noise level of $0.27 \text{ mJy beam}^{-1}$. FIRST J142739.694+330744.45 is undetected with the VLBA and is identified in the optical I band.

FIRST J142744.441+333828.62: The VLBA image in Fig. 3 has a 1σ noise level of $0.37 \text{ mJy beam}^{-1}$. There is a counterpart in the optical I band so this VLBA detection will help link data for the Boötes field to the ICRF.

FIRST J142758.722+324741.56: The FIRST source is the central component of an NVSS double with the tabulated S_I . This NVSS double shows an east-west, Fanaroff-Riley II structure in the FIRST image. The VLBA image in Fig. 3 has a 1σ noise level of $0.43 \text{ mJy beam}^{-1}$. There is a counterpart in the optical I band so this VLBA detection will help link data for the Boötes field to the ICRF.

FIRST J142806.696+325935.83: The VLBA image in Fig. 3 has a 1σ noise level of $0.53 \text{ mJy beam}^{-1}$. There is a counterpart in the optical I band so this VLBA detection will help link data for the Boötes field to the ICRF.

FIRST J142842.556+354326.60: The VLBA images in Fig. 3 from segments 1 and 2 have 1σ noise levels of 0.24 and $0.30 \text{ mJy beam}^{-1}$, respectively. There is a counterpart in the optical I band so this VLBA detection will help link data for the Boötes field to the ICRF.

FIRST J142904.545+343243.54: The NVSS catalog notes a complex source structure. The NVSS image shows a weak extension to the north-east, likely related to a weak secondary in the FIRST image in the same quadrant.

FIRST J142905.105+342641.06: The VLBA images in Fig. 3 from segments 2 and 4 have 1σ noise levels of 0.31 and $0.29 \text{ mJy beam}^{-1}$, respectively. The integrated flux density and the diffuse structure are repeatable between the two segments, but the VLBA image fidelity is likely to be quite poor. On VLA scales at 1.4 GHz, this is among the strongest FIRST sources and its compactness ratio is unity. There is a counterpart in the optical I band so this VLBA detection will help link data for the Boötes field to the ICRF.

FIRST J142910.223+352946.86: The VLBA images in Fig. 4 from segments 1 and 2 have 1σ noise levels of 0.44 and 0.35 mJy beam $^{-1}$, respectively. Garrett et al. (2005) present a VLBI image at 1.4 GHz. There is a counterpart in the optical I band so this VLBA/VLBI detection will help link data for the Boötes field to the ICRF.

FIRST J142911.747+333144.24: The FIRST image shows a weak secondary to the south of the FIRST position.

FIRST J142937.566+344115.69: An NVSS secondary is also present, with $S_I = 3.4 \pm 0.5$ mJy offset by 86" at PA -90° , perhaps related to a weak secondary in the FIRST image in a similar PA. The VLBA image in Fig. 4 has a 1σ noise level of 0.26 mJy beam $^{-1}$ and is the basis for the provisional VLBA detection from segment 1. The less sensitive search from segment 2 resulted in a nondetection. There is a counterpart in the optical I band so this provisional VLBA detection might help link data for the Boötes field to the ICRF.

FIRST J143022.337+343727.14: The FIRST image shows a secondary to the east of the FIRST position.

FIRST J143056.092+341930.18: The FIRST image shows a secondary in the north-west quadrant.

FIRST J143109.858+335301.67: An NVSS secondary is also present, with $S_I = 2.3 \pm 0.4$ mJy offset by 82" at PA 103° .

FIRST J143121.320+332808.95: The VLBA image in Fig. 4 has a 1σ noise level of 0.30 mJy beam $^{-1}$. This image shows either a double or a core-jet structure. There is no counterpart in the optical I band.

FIRST J143123.297+331625.82: The VLBA image in Fig. 4 has a 1σ noise level of 0.30 mJy beam $^{-1}$ and is the basis for the provisional VLBA detection. There is no counterpart in the optical I band catalog but the I band image shows an object 1" to the east.

FIRST J143134.549+351511.19: The NVSS catalog notes a complex source structure. The NVSS image shows a weak extension to the south-east, likely related to a weak secondary in the FIRST image in the same quadrant.

FIRST J143152.544+340110.15: The VLBA images in Fig. 4 from segments 2 and 4 have 1σ noise levels of 0.30 and 0.27 mJy beam $^{-1}$, respectively. The integrated flux density and the double or core-jet structure are repeatable between the two segments. There is a counterpart in the optical I band so this VLBA detection will help link data for the Boötes field to the ICRF.

FIRST J143309.671+351520.14: The FIRST image shows a secondary in the south-east quadrant.

FIRST J143311.054+335828.81: The VLBA image in Fig. 4 has a 1σ noise level of $0.23\text{ mJy beam}^{-1}$. There is a counterpart in the optical I band so this VLBA detection will help link data for the Boötes field to the ICRF.

FIRST J143345.947+341149.03: An NVSS secondary is also present, with $S_I = 100.2 \pm 3.6\text{ mJy}$ offset by $77''$ at PA -102° , perhaps related to a secondary in the south-west quadrant of the FIRST image. There is no counterpart in the optical I band so FIRST J143345.947+341149.03 might be a lobe hotspot.

FIRST J143432.836+352141.47: The FIRST image shows a secondary in the south-east quadrant.

FIRST J143434.217+351009.53: The VLBA image in Fig. 4 has a 1σ noise level of $0.69\text{ mJy beam}^{-1}$. There is a counterpart in the optical I band so this VLBA detection will help link data for the Boötes field to the ICRF.

FIRST J143445.321+332820.58: The VLBA image in Fig. 4 has a 1σ noise level of $0.27\text{ mJy beam}^{-1}$. It was formed from phase self-calibrated data, yielded the tabulated VLBA flux density, and was used to estimate a coherence correction for segment 4. The phase-referenced image yielded the tabulated VLBA position and was used to estimate a coherence correction for segment 4. There is a counterpart in the optical I band so this VLBA detection will help link data for the Boötes field to the ICRF.

FIRST J143446.491+332452.27: The VLBA image in Fig. 4 has a 1σ noise level of $0.25\text{ mJy beam}^{-1}$ and is the basis for the provisional VLBA detection. There is a counterpart in the optical I band so this provisional VLBA detection might help link data for the Boötes field to the ICRF.

FIRST J143449.111+354246.98: The NVSS image shows an asymmetry to the east, seemingly related to the eastern secondary in the FIRST image. The VLBA image in Fig. 4 has a 1σ noise level of $0.38\text{ mJy beam}^{-1}$ and in Fig. 5 has a 1σ noise level of $0.30\text{ mJy beam}^{-1}$. The integrated flux density and the double or core-jet structure are repeatable between the two segments. There is a counterpart in the optical I band so this VLBA detection will help link data for the Boötes field to the ICRF.

FIRST J143527.951+331145.46: The NVSS image shows an asymmetry to the south-east, seemingly related to the weak secondary in the same quadrant of the FIRST image. The VLBA image in Fig. 5 has a 1σ noise level of $0.23\text{ mJy beam}^{-1}$ and is the basis for the provisional VLBA detection. There is a counterpart in the optical I band so this

provisional VLBA detection might help link data for the Boötes field to the ICRF.

FIRST J143528.374+331931.53: The VLBA image in Fig. 5 has a 1σ noise level of $0.36\text{ mJy beam}^{-1}$. There is a counterpart in the optical I band so this VLBA detection will help link data for the Boötes field to the ICRF.

FIRST J143529.161+343422.94: The VLBA image in Fig. 5 has a 1σ noise level of $0.24\text{ mJy beam}^{-1}$. There is a counterpart in the optical I band so this VLBA detection will help link data for the Boötes field to the ICRF.

FIRST J143543.629+353305.02: The FIRST image shows a secondary in the north-west quadrant.

FIRST J143643.209+352222.98: The VLBA image in Fig. 5 has a 1σ noise level of $0.32\text{ mJy beam}^{-1}$. There is no counterpart in the optical I band.

FIRST J143647.710+331037.66: The FIRST image shows a secondary to the south.

FIRST J143713.571+350554.84: The VLBA image in Fig. 5 has a 1σ noise level of $0.54\text{ mJy beam}^{-1}$. There is a counterpart in the optical I band so this VLBA detection will help link data for the Boötes field to the ICRF.

FIRST J143723.715+350734.69: The NVSS catalog notes a complex source structure. The NVSS image shows this is likely due to the proximity of an NVSS secondary, cataloged as having $S_I = 14.6 \pm 0.6\text{ mJy}$ offset by $70''$ at PA 78° .

FIRST J143728.413+331110.20: An NVSS secondary is also present, with $S_I = 8.2 \pm 0.5\text{ mJy}$ offset by $77''$ at PA 23° . The VLBA image in Fig. 5 has a 1σ noise level of $0.31\text{ mJy beam}^{-1}$.

FIRST J143752.050+351940.08: The NVSS catalog notes a complex source structure. The NVSS image shows this is likely due to the proximity of an NVSS secondary, cataloged as having $S_I = 96.8 \pm 3.8\text{ mJy}$ offset by $53''$ at PA 90° . The VLBA image in Fig. 5 has a 1σ noise level of $0.28\text{ mJy beam}^{-1}$ and shows either a double or a core-jet structure. There is a counterpart in the optical I band so this VLBA detection will help link data for the Boötes field to the ICRF.

FIRST J143841.949+335809.48: The VLBA image in Fig. 5 has a 1σ noise level of $0.30\text{ mJy beam}^{-1}$ and shows either a double or a core-jet structure. There is a counterpart in the optical I band so this VLBA detection will help link data for the Boötes field to the ICRF.

FIRST J143850.267+340419.84: The VLBA image in Fig. 5 has a 1σ noise level of 0.28 mJy beam $^{-1}$. The identification status is based on the R band, as the I band data are corrupted or missing.

FIRST J143859.469+345309.33: The FIRST image shows a secondary in the north-east quadrant. The identification status is based on the R band, as the I band data are corrupted or missing.

FIRST J143909.406+332101.73: The FIRST source appears to be associated with the stronger component of the compact NVSS double with the tabulated S_I . The NVSS catalog notes a complex source structure for both components of the double, but areal integration over the NVSS image confirms the tabulated S_I . The VLBA image in Fig. 5 has a 1σ noise level of 0.34 mJy beam $^{-1}$.

FIRST J143916.249+344912.09: The VLBA image in Fig. 5 has a 1σ noise level of 0.34 mJy beam $^{-1}$.

REFERENCES

Beasley, A. J., Gordon, D., Peck, A. B., Petrov, L., MacMillian, D. S., Fomalont, E. B., & Ma, C. 2002, ApJS, 141, 13

Condon, J. J., Cotton, W. D., Greisen, E. W., Yin, Q. F., Perley, R. A., Taylor, G. B., & Broderick, J. J. 1998, AJ, 115, 1693

Condon, J. J. 1999, Proc. Natl. Acad. Sci., 96, 4756

Condon, J. J., Cotton, W. D., Yin, Q. F., Shupe, D. L., Storrie-Lombardi, L. J., Helou, G., Soifer, B. T., & Werner, M. W. 2003, AJ, 125, 2411

Cristiani, S., Renzini, A., & Williams, R. E. Deep Fields, ESO Astrophysics Symposia, (Springer-Verlag: Heidelberg)

Dey, A., et al. 2005, ApJ, submitted

Eisenhardt, P. R., et al. 2004, ApJS, 154, 48

Fomalont, E. B., Petrov, L., MacMillian, D. S., Gordon, D., & Ma, C. 2003, AJ, 126, 2562

Garrett, M. A., & Garrington, S. T. 1998, in ASP Conf. Ser. 144, ed. J. A. Zensus, G. B. Taylor, & J. M. Wrobel (San Francisco: ASP), 145

Garrett, M. A., Wrobel, J. M., & Morganti, R. 2005, ApJ, 619, 105

Gehrels, N. 1986, ApJ, 303, 336

Higdon, J. L., et al. 2005, ApJ, 626, 58

IERS. 1999, 1998 Annual Report, ed. D. Gambis (Paris: Obs. Paris), 87

Giovannini, G., Taylor, G. B., Feretti, L., Cotton, W. D., Lara, L. & Venturi, T., 2005, ApJ, 618, 635

Houck, J. R., et al. 2005, ApJ, 622, 105

Jannuzzi, B. T., & Dey, A. 1999, in ASP Conf. Ser. Vol. 191, Photometric Redshifts and High Redshift Galaxies, ed. R. J. Weymann et al. (San Francisco: ASP), 111

Jannuzzi, B. T., et al. 2005, ApJ, submitted

Kellermann, K. I., et al. 2004, ApJ, 609, 539

Ma, C., et al. 1998, AJ, 116, 516

Myers, S. T., et al. 2003, MNRAS, 341, 1

Napier, P. J., Bagri, D. S., Clark, B. G., Rogers, A. E. E., Romney, J. D., Thompson, A. R., & Walker, R. C. 1994, Proc. IEEE, 82, 658

Petrov, L., Kovalev, Y. Y., Fomalont, E. B., & Gordon, D. 2005, AJ, 129, 1163

Porcas, R. W., Alef, W., Ghosh, T., Salter, C. J., and Garrington, S. T. 2004, in Proceedings of the 7th European VLBI Network Symposium, ed. R. Bachiller, F. Colomer, J.-F. Desmurs, & P. de Vicente (Toledo: Observatorio Astronomico Nacional), 31

Spergel, D. N., et al. 2003, ApJS, 148, 175

Taylor, G. B., Vermeulen, R. C., Readhead, A. C. S., Pearson, T. J., Henstock, D. R., & Wilkinson, P. N. 1996, ApJS, 107, 37

Taylor, G. B., Marr, J. M., Pearson, T. J., & Readhead, A. C. S. 2000, ApJ, 541, 112

Taylor, G. B., et al., 2005, ApJS, 159, 27

Vermeulen, R. C., Britzen, S., Taylor, G. B., Pearson, T. J., Readhead, A. C. S., Wilkinson, P. N., & Browne, I. W. A. 2003, in ASP Conf. Ser. 300, Radio Astronomy at the Fringe, ed. J. A. Zensus, M. H. Cohen, & E. Ros (San Francisco: ASP), 43

Wang, J. X., et al. 2004, AJ, 127, 213

White, R. L., Becker, R. H., Helfand, D. J., & Gregg, M. D. 1997, ApJ, 475, 479

Wilkinson, P. N., et al. 2001, Phys. Rev. Lett., 86, 584

Wrobel, J. M. 1995, in ASP Conf. Ser. 82, Very Long Baseline Interferometry and the VLBA, ed. J. A. Zensus, P. J. Diamond, & P. J. Napier (San Francisco: ASP), 413

Wrobel, J. M., Walker, R. C., Benson, J. M., & Beasley, A. J. 2000, VLBA Scientific Memo 24

Wrobel, J. M., Garrett, M. A., Condon, J. J., & Morganti, R. 2004, AJ, 128, 103

Xu, C., Baum, S. A., O'Dea, C. P., Wrobel, J. M., & Condon, J. J. 2000, AJ, 120, 2950

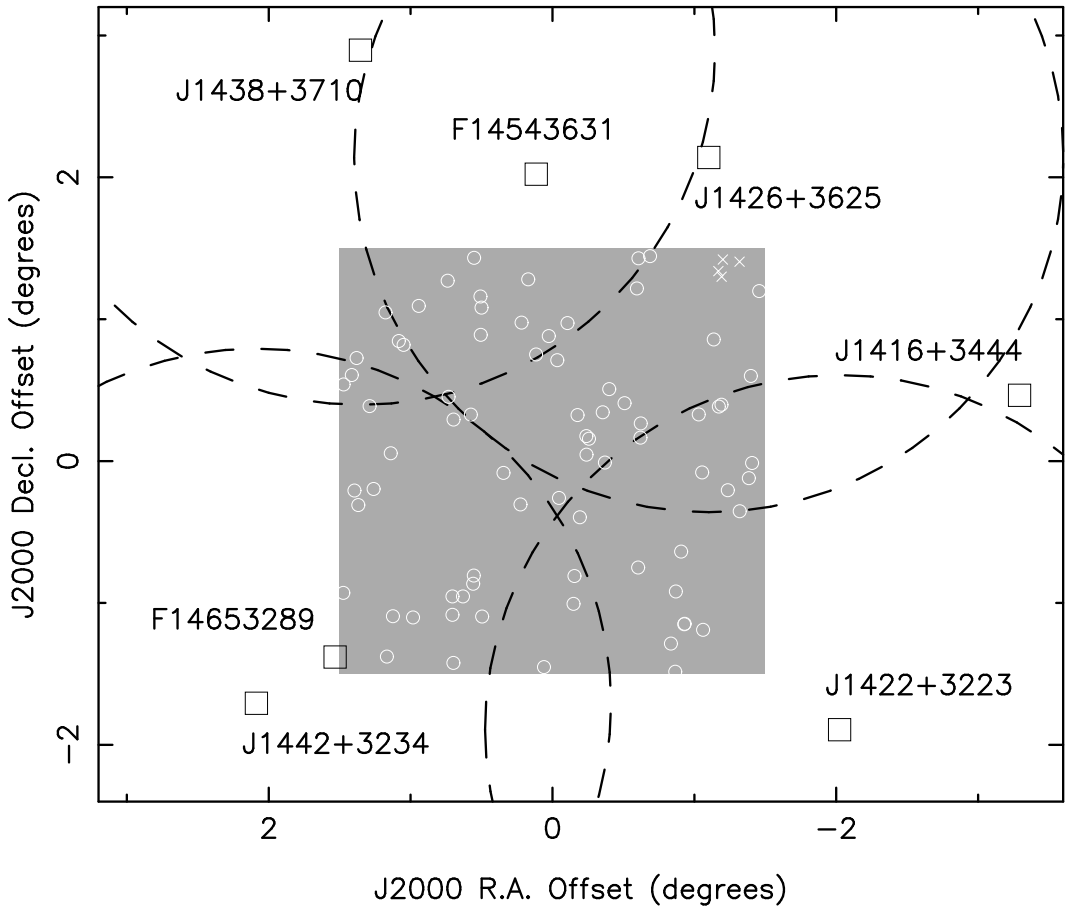


Fig. 1.— Geometry for the VLBA observations at 5.0 GHz within the NOAO Boötes field, shown as a grey square covering 9.0 deg^2 . Light circles show the locations of the FIRST sources listed in Table 1. Dark squares show the locations of calibrator sources, four of which served as phase calibrators for the VLBA observations of FIRST sources within the large dashed circles, each of radius 2.5° . Crosses in north-east corner of the Boötes field show the four X-ray sources from Wang et al. with FIRST counterparts, all weaker than 10 mJy.

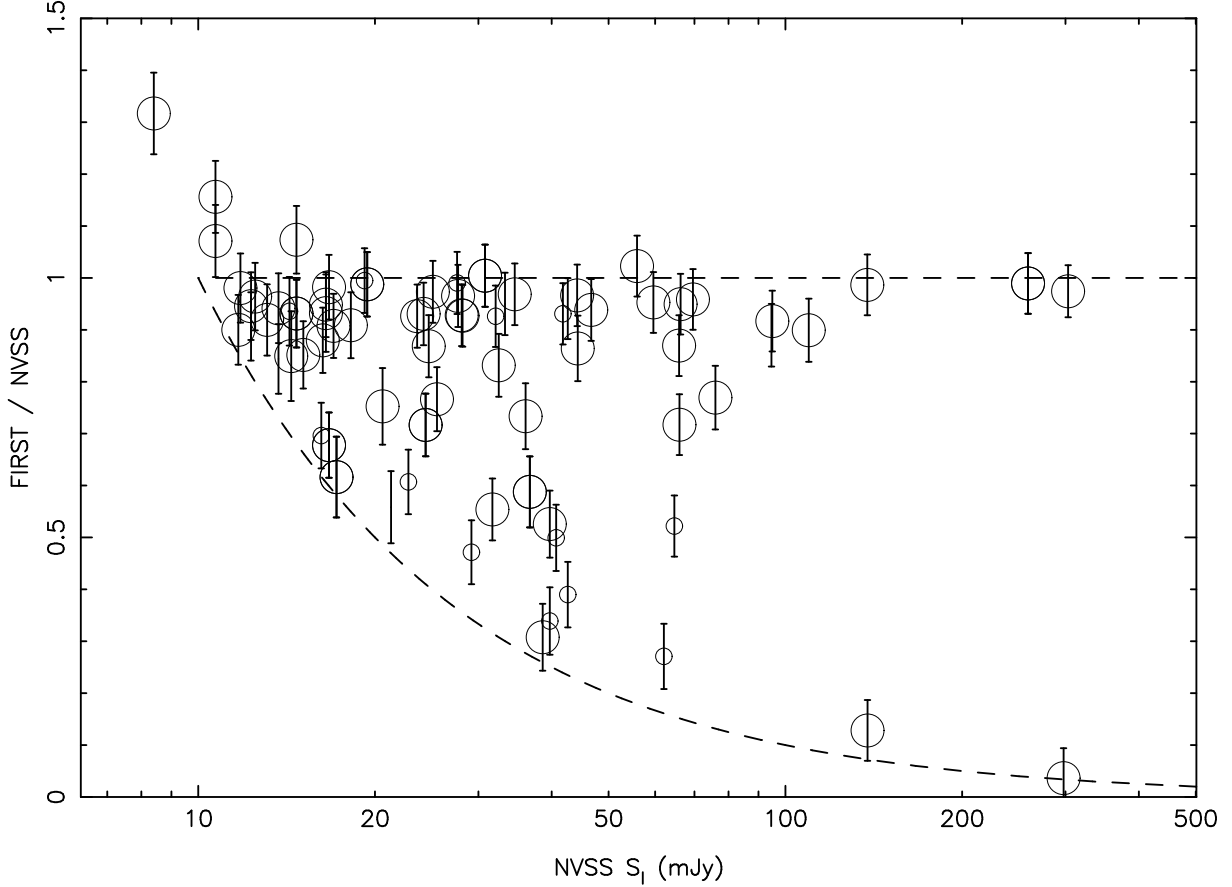


Fig. 2.— Ordinate is the ratio at 1.4 GHz of the peak flux density at 5'' resolution from FIRST to the integrated flux density at 45'' resolution from the NVSS. This ratio is a measure of the compactness of the FIRST source. Abscissa is the integrated NVSS flux density. The dashed horizontal line corresponds to a source whose peak FIRST flux density and integrated NVSS flux density are equal, and have a value of 10 mJy or more. The dashed curved line corresponds to a source whose peak FIRST flux density is 10 mJy, while its integrated NVSS flux density is 10 mJy or more. A large circle means the FIRST source is identified in the optical I band, while a small circle means it is unidentified.

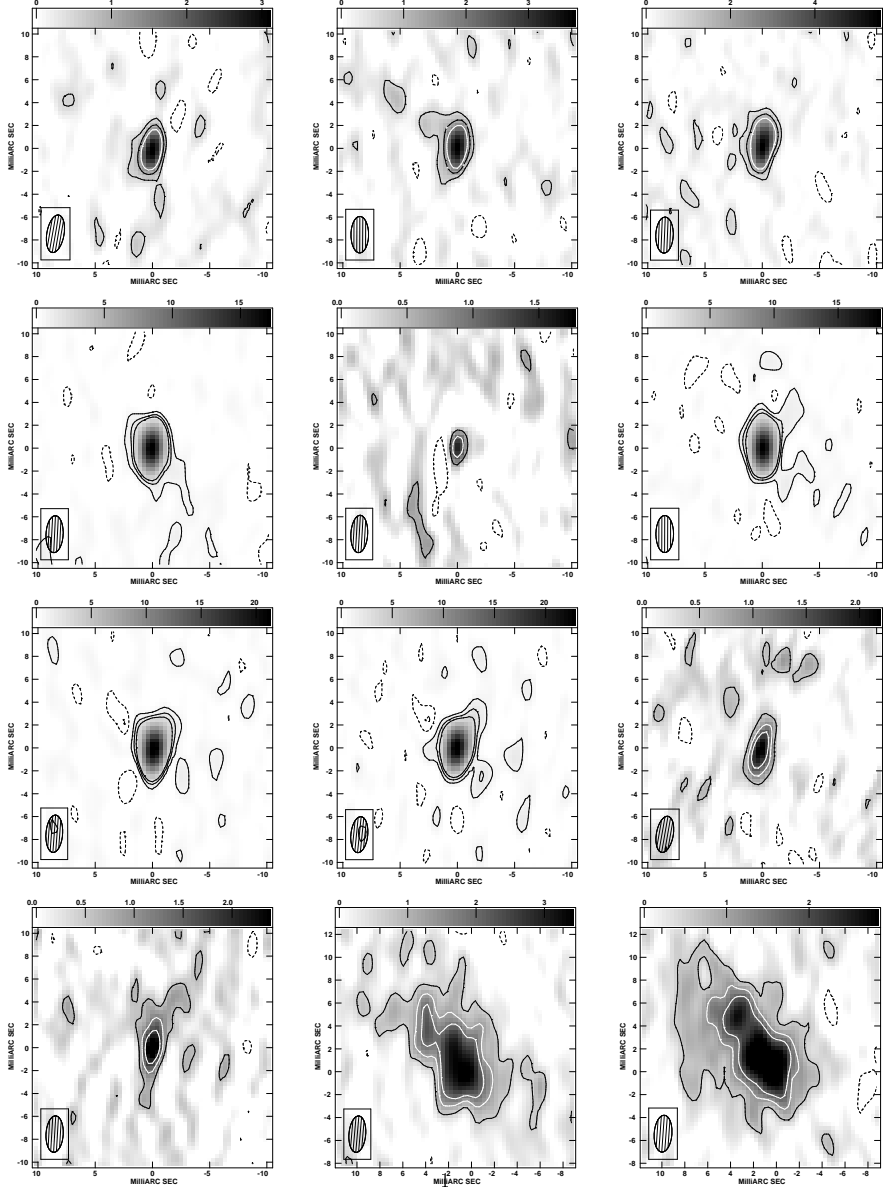


Fig. 3.— Phase-referenced and cleaned images at 5.0 GHz of Stokes I emission for FIRST sources detected with the NRAO VLBA within a square search region of side 1400 mas. The boxed ellipse shows the Gaussian restoring beam at FWHM. Contours are at ± 2 , ± 4 , and ± 6 times the 1σ noise level quoted in the appendix. *Left to right, from the top:* FIRST J142456.287+352841.80 (segment 1), FIRST J142456.287+352841.80 (segment 2), FIRST J142524.214+340935.68, FIRST J142607.716+340426.29, FIRST J142738.625+330756.96, FIRST J142744.441+333828.62, FIRST J142758.722+324741.56, FIRST J142806.696+325935.83, FIRST J142842.556+354326.60 (segment 1), FIRST J142842.556+354326.60 (segment 2), FIRST J142905.105+342641.06 (segment 2), FIRST J142905.105+342641.06 (segment 4).

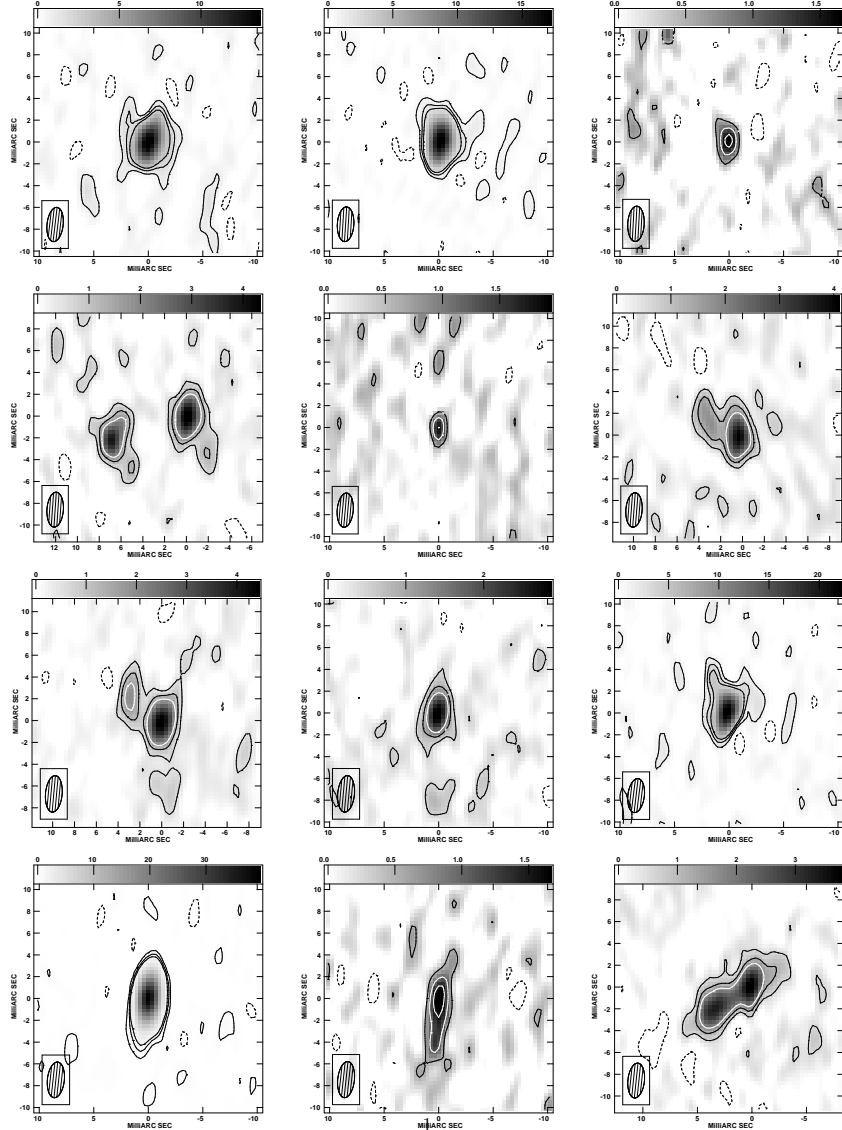


Fig. 4.— Same as Fig. 3, but for FIRST J142910.223+352946.86 (segment 1), FIRST J142910.223+352946.86 (segment 2), FIRST J142937.566+344115.69, FIRST J143121.320+332808.95, FIRST J143123.297+331625.82, FIRST J143152.544+340110.15 (segment 2), FIRST J143152.544+340110.15 (segment 4), FIRST J143311.054+335828.81, FIRST J143434.217+351009.53, FIRST J143445.321+332820.58, FIRST J143446.491+332452.27, FIRST J143449.111+354246.98 (segment 1) .

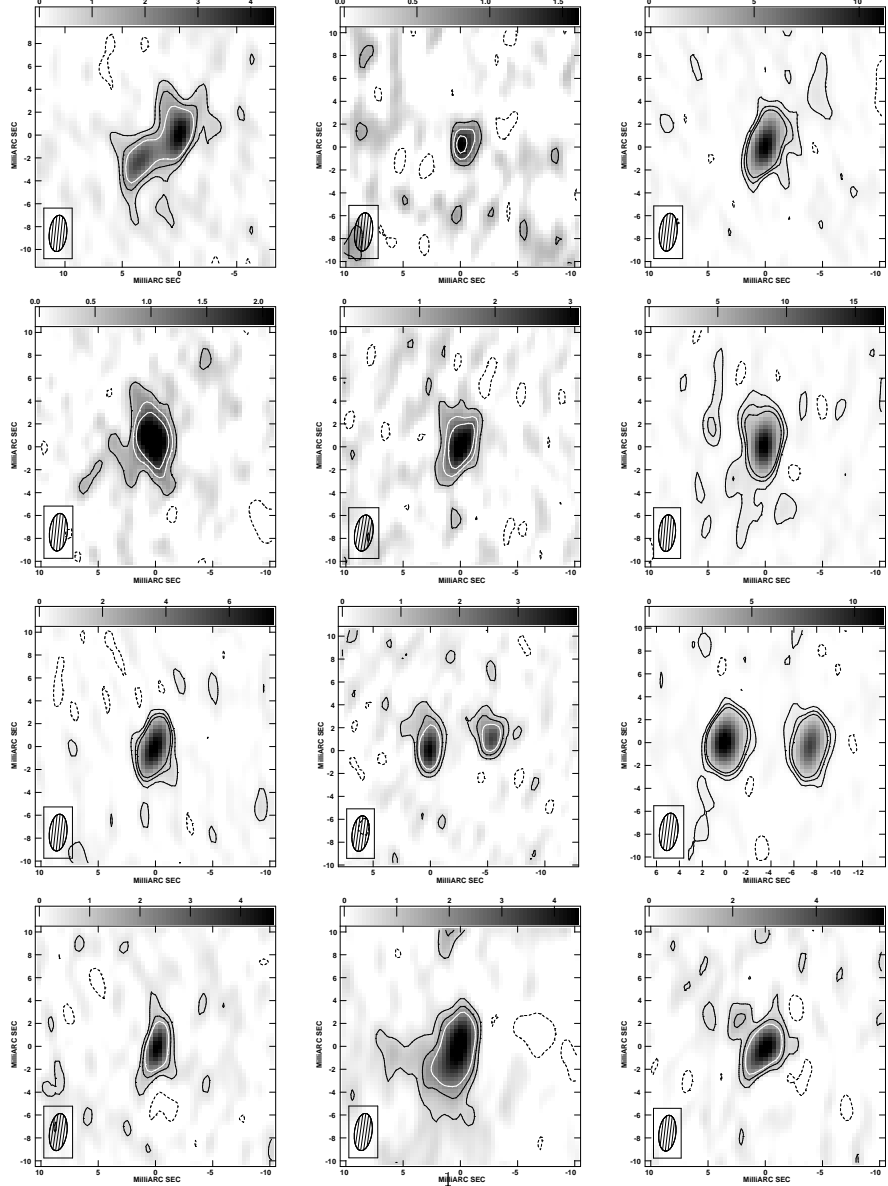


Fig. 5.— Same as Fig. 3, but for FIRST J143449.111+354246.98 (segment 2), FIRST J143527.951+331145.46, FIRST J143528.374+331931.53, FIRST J143529.161+343422.94, FIRST J143643.209+352222.98, FIRST J143713.571+350554.84, FIRST J143728.413+331110.20, FIRST J143752.050+351940.08, FIRST J143841.949+335809.48, FIRST J143850.267+340419.84, FIRST J143909.406+332101.73, FIRST J143916.249+344912.09.

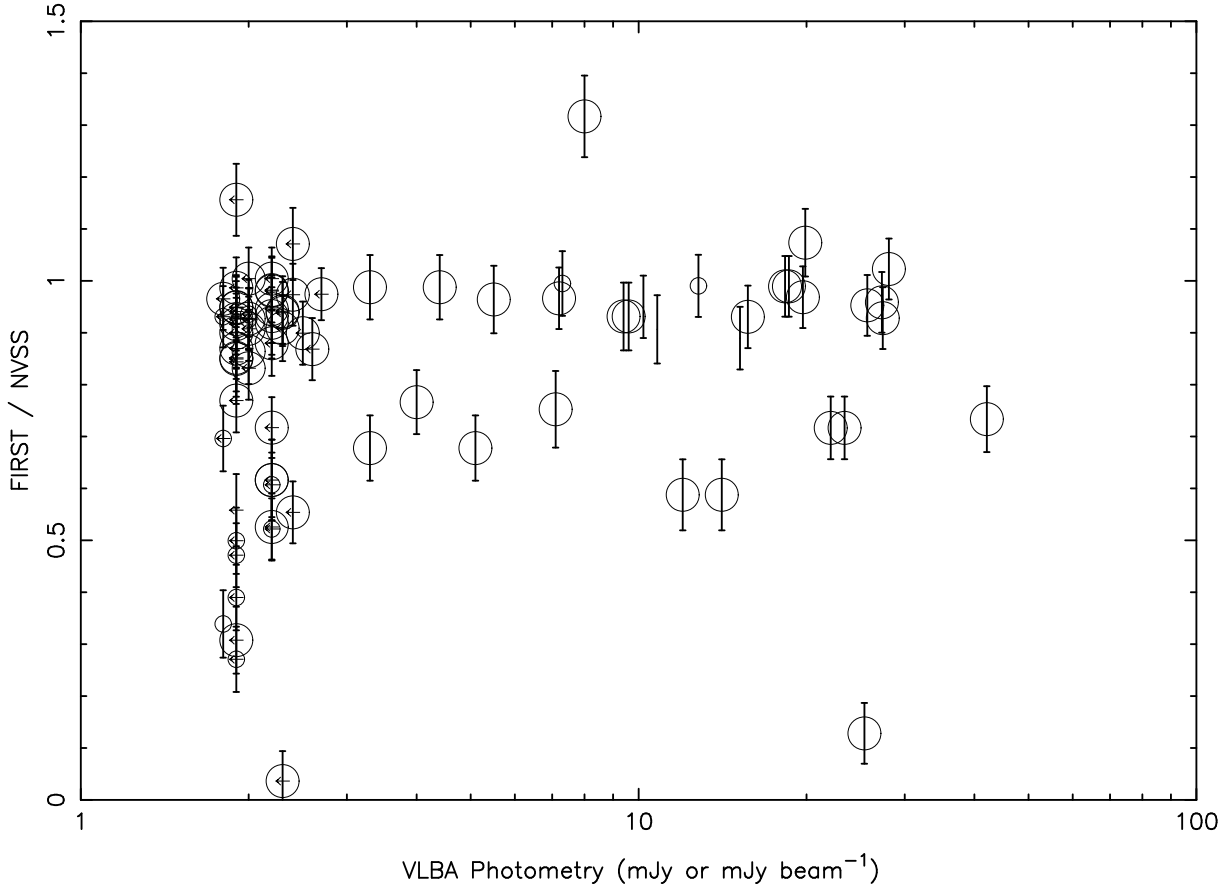


Fig. 6.— Ordinate is the ratio at 1.4 GHz of the peak flux density at 5'' resolution from FIRST to the integrated flux density at 45'' resolution from the NVSS. This ratio is a measure of the compactness of the FIRST source. Abscissa quantifies the VLBA photometry at 5.0 GHz, corresponding to the integrated flux density for VLBA detections, the peak flux density for provisional VLBA detections, or upper limits to the peak flux density for VLBA nondetections. A large circle means the FIRST source is identified in the optical *I* band, while a small circle means it is unidentified.

Table 1. Faint Sources with Deconvolved Major Diameters Less Than 3" in FIRST

FIRST Name (1)	VLA at 1.4 GHz				VLBA at 5.0 GHz					
	FIRST Peak S_P (mJy beam $^{-1}$) (2)	NVSS Integrated S_I (mJy) (3)	ID ^a (4)	Seg- ment (5)	Search Image σ (mJy beam $^{-1}$) (6)	R.A. (J2000.0) (7)	Decl. (J2000.0) (8)	Integrated S_I (mJy) (9)	Note ^b (10)	
J142456.287+352841.80	11.32 ± 0.583	16.7 ± 0.6	i	1	0.27	14 24 56.3046	+35 28 41.747	3.3 ± 0.5	*	
J142456.287+352841.80	11.32 ± 0.583	16.7 ± 0.6	i	2	0.35	14 24 56.3046	+35 28 41.747	5.1 ± 0.7	*	
J142516.512+345246.62	57.30 ± 2.868	65.9 ± 2.0	i	1	0.26	$<1.9^c$		
J142517.227+341559.33	14.34 ± 0.730	16.3 ± 0.6	i	2	0.31	$<2.2^c$		
J142524.214+340935.68	15.50 ± 0.790	20.6 ± 1.1	i	2	0.37	14 25 24.2201	+34 09 35.889	7.1 ± 0.7	*	
J142543.885+335533.24	295.30 ± 14.766	303.1 ± 0.9	i	2	0.38	$<2.7^c$		
J142607.716+340426.29	33.51 ± 1.682	34.6 ± 1.1	i	2	0.60	14 26 07.7162	+34 04 26.325	19.7 ± 1.2	*	
J142617.948+344039.63	11.88 ± 0.611	38.6 ± 1.5	i	1	0.27	$<1.9^c$	*	
J142623.374+343950.45	16.61 ± 0.842	42.6 ± 1.6	u	1	0.27	$<1.9^c$	*	
J142632.164+350814.71	87.10 ± 4.357	95.0 ± 2.9	i	1	0.27	$<1.9^c$		
J142659.719+341200.21	10.80 ± 0.557	297.7 ± 7.7	i	2	0.32	$<2.3^c$	*	
J142701.644+330524.96	16.54 ± 0.834	18.2 ± 0.7	i	3a	0.32	$<2.3^c$		
J142705.073+343628.84	27.03 ± 1.358	32.5 ± 1.1	i	1	0.28	$<2.0^c$		
J142738.625+330756.96	13.46 ± 0.684	39.7 ± 1.6	u	3a	0.29	14 27 38.5713	+33 07 56.723	1.8 ± 0.3^c	*	
J142739.694+330744.45	20.87 ± 1.051	39.7 ± 1.6	i	3a	0.31	$<2.2^c$	*	
J142744.441+333828.62	15.78 ± 0.801	14.7 ± 0.6	i	3a	0.57	14 27 44.4413	+33 38 28.603	19.9 ± 1.2	*	
J142755.936+332139.92	15.43 ± 0.783	17.0 ± 0.6	i	3a	0.28	$<2.0^c$		
J142758.722+324741.56	17.70 ± 0.893	138.0 ± 4.1	i	3a	0.70	14 27 58.7263	+32 47 41.474	25.4 ± 1.5	*	
J142806.696+325935.83	26.08 ± 1.310	28.1 ± 0.9	i	3a	0.72	14 28 06.7043	+32 59 35.781	27.4 ± 1.7	*	
J142842.556+354326.60	19.16 ± 0.968	19.4 ± 0.7	i	1	0.27	14 28 42.5556	+35 43 26.942	3.3 ± 0.6	*	
J142842.556+354326.60	19.16 ± 0.968	19.4 ± 0.7	i	2	0.33	14 28 42.5556	+35 43 26.942	4.4 ± 0.8	*	
J142904.545+343243.54	12.23 ± 0.628	14.4 ± 1.0	i	1	0.26	$<1.9^c$	*	
J142905.105+342641.06	256.22 ± 12.812	259.0 ± 7.8	i	2	0.42	14 29 05.1184	+34 26 40.997	18.6 ± 1.4	*	
J142905.105+342641.06	256.22 ± 12.812	259.0 ± 7.8	i	4	0.34	14 29 05.1182	+34 26 40.996	18.3 ± 1.3	*	
J142906.607+354234.67	29.73 ± 1.493	32.1 ± 1.0	u	1	0.28	$<2.0^c$		
J142910.223+352946.86	17.49 ± 0.886	24.4 ± 0.8	i	1	0.50	14 29 10.2224	+35 29 46.891	22.1 ± 1.5	*	
J142910.223+352946.86	17.49 ± 0.886	24.4 ± 0.8	i	2	0.63	14 29 10.2224	+35 29 46.891	23.4 ± 1.4	*	
J142911.747+333144.24	47.34 ± 2.371	66.0 ± 2.0	i	3a	0.30	$<2.2^c$	*	
J142937.566+344115.69	10.60 ± 0.547	17.2 ± 1.0	i	1	0.27	14 29 37.5549	+34 41 15.591	2.2 ± 0.3^c	*	

Table 1—Continued

VLA at 1.4 GHz				VLBA at 5.0 GHz						
FIRST Name	FIRST Peak S_P (mJy beam $^{-1}$)	NVSS Integrated S_I (mJy)	ID ^a	Seg-ment	Search Image σ (mJy beam $^{-1}$)	R.A. (J2000.0)	Decl. (J2000.0)	Integrated S_I (mJy)	Note ^b	
(1)	(2)	(3)	(4)	(5)	(6)	(7)	(8)	(9)	(10)	
J142937.566+344115.69	10.60 ± 0.547	17.2 ± 1.0	i	2	0.31	<2.2 ^c	*	
J143008.885+344713.75	26.74 ± 1.345	27.7 ± 0.9	i	1	0.25	<1.8 ^c		
J143018.550+341611.65	11.57 ± 0.595	11.8 ± 0.5	i	2	0.30	<2.2 ^c		
J143022.337+343727.14	11.28 ± 0.579	16.2 ± 0.6	u	1	0.25	<1.8 ^c	*	
J143050.912+342614.17	11.46 ± 0.589	10.7 ± 0.5	i	2	0.34	<2.4 ^c		
J143056.092+341930.18	33.77 ± 1.694	64.7 ± 2.0	u	2	0.31	<2.2 ^c	*	
J143056.256+342722.42	12.90 ± 0.659	13.7 ± 0.6	i	2	0.32	<2.3 ^c		
J143109.858+335301.67	26.14 ± 1.313	28.2 ± 0.9	i	3a	0.28	<2.0 ^c	*	
J143114.097+343616.43	16.40 ± 0.834	16.7 ± 0.6	i	2	0.31	<2.2 ^c		
J143121.320+332808.95	27.33 ± 1.373	27.6 ± 0.9	u	3a	0.35	14 31 21.3546	+33 28 08.744	12.8 ± 1.2	*	
J143123.297+331625.82	15.38 ± 0.781	16.5 ± 0.9	i	3a	0.31	14 31 23.3356	+33 16 25.880	2.2 ± 0.3 ^c	*	
J143134.549+351511.19	58.47 ± 2.927	76.0 ± 2.7	i	1	0.27	<1.9 ^c	*	
J143152.544+340110.15	13.69 ± 0.698	14.7 ± 0.6	i	2	0.36	14 31 52.5521	+34 01 09.990	9.6 ± 1.1	*	
J143152.544+340110.15	13.69 ± 0.698	14.7 ± 0.6	i	4	0.30	14 31 52.5520	+34 01 09.990	9.4 ± 0.9	*	
J143155.856+345926.99	10.53 ± 0.545	11.7 ± 0.5	i	1	0.27	<1.9 ^c		
J143213.543+350941.05	15.65 ± 0.796	16.5 ± 0.6	i	1	0.27	<1.9 ^c		
J143222.785+324939.62	11.63 ± 0.592	12.3 ± 0.5	i	3a	0.31	<2.2 ^c		
J143239.561+350151.42	12.86 ± 0.659	15.1 ± 0.6	i	1	0.26	<1.9 ^c		
J143256.072+353339.52	62.94 ± 3.150	66.3 ± 2.0	i	1	0.27	<1.9 ^c		
J143309.671+351520.14	13.77 ± 0.704	29.2 ± 1.0	u	1	0.26	<1.9 ^c	*	
J143311.054+335828.81	19.54 ± 0.987	25.5 ± 0.9	i	4	0.25	14 33 11.0825	+33 58 28.533	4.0 ± 0.5	*	
J143345.947+341149.03	16.82 ± 0.852	62.1 ± 2.3	u	4	0.26	<1.9 ^c	*	
J143428.007+331102.05	21.86 ± 1.103	23.6 ± 0.8	i	4	0.26	<1.9 ^c		
J143432.836+352141.47	20.32 ± 1.024	40.7 ± 1.6	u	1	0.26	<1.9 ^c	*	
J143434.217+351009.53	66.72 ± 3.339	69.6 ± 2.1	i	2	0.77	14 34 34.2216	+35 10 09.432	27.3 ± 1.9	*	
J143435.361+352622.26	30.93 ± 1.552	30.8 ± 1.0	i	1	0.28	<2.0 ^c		
J143435.361+352622.26	30.93 ± 1.552	30.8 ± 1.0	i	2	0.30	<2.2 ^c		
J143445.321+332820.58	26.48 ± 1.331	36.1 ± 1.4	i	4	0.97	14 34 45.3500	+33 28 20.571	42.1 ± 2.2	*	
J143446.491+332452.27	12.04 ± 0.616	13.1 ± 0.6	i	4	0.27	14 34 46.5226	+33 24 52.151	2.2 ± 0.3 ^c	*	

Table 1—Continued

VLA at 1.4 GHz				VLBA at 5.0 GHz						
FIRST Name	FIRST Peak S_P (mJy beam $^{-1}$)	NVSS Integrated S_I (mJy)	ID ^a	Seg-ment	Search Image σ (mJy beam $^{-1}$)	R.A. (J2000.0)	Decl. (J2000.0)	Integrated S_I (mJy)	Note ^b	
(1)	(2)	(3)	(4)	(5)	(6)	(7)	(8)	(9)	(10)	
J143449.111+354246.98	21.57 ± 1.088	36.7 ± 1.7	i	1	0.32	14 34 49.1016	+35 42 47.221	12.0 ± 1.1	*	
J143449.111+354246.98	21.57 ± 1.088	36.7 ± 1.7	i	2	0.38	14 34 49.1016	+35 42 47.221	14.1 ± 1.3	*	
J143453.497+343626.65	24.43 ± 1.230	25.1 ± 0.8	i	2	0.34	<2.4 ^c		
J143507.129+331933.55	13.38 ± 0.683	14.3 ± 0.6	u	4	0.28	<2.0 ^c		
J143525.184+325124.06	11.56 ± 0.587	13.7 ± 0.6	...	4	0.26	<1.9 ^c		
J143527.951+331145.46	38.28 ± 1.918	44.3 ± 1.7	i	4	0.26	14 35 27.9710	+33 11 45.456	2.0 ± 0.3 ^c	*	
J143528.374+331931.53	22.52 ± 1.135	24.2 ± 0.8	i	4	0.41	14 35 28.3946	+33 19 31.464	15.7 ± 1.1	*	
J143529.161+343422.94	42.71 ± 2.140	44.2 ± 1.4	i	4	0.27	14 35 29.1470	+34 34 22.721	7.2 ± 0.9	*	
J143539.740+344359.55	21.45 ± 1.081	24.7 ± 0.8	i	2	0.36	<2.6 ^c		
J143543.629+353305.02	17.56 ± 0.888	31.7 ± 1.0	i	2	0.34	<2.4 ^c	*	
J143643.209+352222.98	19.10 ± 0.965	19.2 ± 0.7	u	2	0.38	14 36 43.2194	+35 22 22.963	7.3 ± 1.0	*	
J143647.710+331037.66	11.89 ± 0.609	21.3 ± 1.0	...	4	0.26	<1.9 ^c	*	
J143713.571+350554.84	56.78 ± 2.843	59.6 ± 1.8	i	3b	0.66	14 37 13.5686	+35 05 54.832	25.7 ± 1.8	*	
J143723.715+350734.69	98.55 ± 4.930	109.6 ± 3.8	i	3b	0.35	<2.5 ^c	*	
J143728.413+331110.20	11.15 ± 0.577	12.3 ± 0.5	...	4	0.35	14 37 28.4307	+33 11 10.069	10.8 ± 0.8	*	
J143737.176+342006.52	38.91 ± 1.950	41.8 ± 1.3	u	4	0.25	<1.8 ^c		
J143739.458+325408.08	40.08 ± 2.007	42.6 ± 1.3	...	4	0.27	<1.9 ^c		
J143752.050+351940.08	11.06 ± 0.568	8.4 ± 0.5	i	3b	0.34	14 37 52.0516	+35 19 39.965	8.0 ± 0.9	*	
J143811.062+340459.63	136.04 ± 6.804	137.9 ± 4.2	i	4	0.27	<1.9 ^c		
J143821.829+344001.06	12.37 ± 0.634	10.7 ± 0.5	i	4	0.26	<1.9 ^c		
J143841.949+335809.48	57.17 ± 2.862	55.9 ± 1.7	i	4	0.48	14 38 41.9460	+33 58 09.504	28.1 ± 1.7	*	
J143850.267+340419.84	12.05 ± 0.618	12.5 ± 0.5	i	4	0.30	14 38 50.2712	+34 04 20.173	5.5 ± 0.6	*	
J143850.280+350021.16	43.82 ± 2.195	46.7 ± 1.5	i	3b	0.32	<2.3 ^c		
J143859.469+345309.33	13.84 ± 0.709	22.8 ± 0.8	u	3b	0.31	<2.2 ^c	*	
J143909.406+332101.73	84.25 ± 4.215	94.7 ± 3.2	...	4	0.35	14 39 09.4176	+33 21 01.674	15.2 ± 1.4	*	
J143916.249+344912.09	31.63 ± 1.589	33.3 ± 1.1	...	3b	0.39	14 39 16.2428	+34 49 11.970	10.2 ± 0.9	*	

| 28 |

Note. — Units of right ascension are hours, minutes, and seconds, and units of declination are degrees, arcminutes, and arcseconds. One-dimensional errors at 1σ are estimated to be 2.5 mas.

^aIdentification status in the *I* band from Jannuzi et al. 2005. i means identified with a galaxy or quasar. u means unidentified.

^bAn * means there is a note on the source in the appendix.

^cPeak flux density at 2 mas resolution after correction for coherence losses. Upper limits are 6σ .

Table 2. Calibrators in Frame of IRCF-Ext.1 Catalog

Calibrator											
VLBA Seg- ment (1)	UT (2)	Epoch	Number of Antennas (3)	Type (4)	Name (5)	R.A. (J2000.0) (6)	Decl. (J2000.0) (7)	Ref. (8)	Switching Angle (°) (9)	Coherence Correc- tion (10)	Position Correc- tion (mas) (11)
1	2001	Apr 26	10	Phase	J1426+3625	14 26 37.08749	+36 25 09.5739	1
				Check	J1416+3444	14 16 04.18624	+34 44 36.4276	1,2	2.7	1.2	-1.2,-0.2
				Check	F14543631	14 32 39.82965	+36 18 07.9321	1	1.2	1.1	+0.2,-1.5
2	2002	Apr 26	9	Phase	J1426+3625	14 26 37.08749	+36 25 09.5739	1
				Check	J1416+3444	14 16 04.18624	+34 44 36.4276	1,2	2.7	1.4	-0.1,-0.3
				Check	J1438+3710	14 38 53.61097	+37 10 35.4168	1,2	2.6	1.2	-0.5,+0.1
				Check	F14543631	14 32 39.82965	+36 18 07.9321	1	1.2	1.1	+0.1,-1.4
3a	2002	Apr 28	9	Phase	J1422+3223	14 22 30.37894	+32 23 10.4405	1
				Check	J1416+3444	14 16 04.18624	+34 44 36.4276	1,2	2.7	1.1	+0.4,-1.0
3b	2002	Apr 28	9	Phase	J1438+3710	14 38 53.61097	+37 10 35.4168	1,2
				Check	J1426+3625	14 26 37.08749	+36 25 09.5739	1	2.6	1.2	+0.2,+0.3
				Check	F14543631	14 32 39.82965	+36 18 07.9321	1	1.5	1.1	-0.6,-1.2
4	2002	Jun 15 ^a	10	Phase	J1442+3234	14 42 00.13897	+32 34 20.3016	1,2
				Check	F14653289	14 39 23.65450	+32 53 54.8237	1	0.6	1.0	+2.3,-0.9

Note. — Units of right ascension are hours, minutes, and seconds, and units of declination are degrees, arcminutes, and arcseconds. One-dimensional errors at 1σ are better than 1 mas for all calibrators except F14653289, for which they are better than 1.3 mas.

^aFIRST J143445.321+332820.58 was also strong enough to phase self-calibrate and thus serve as a coherence check. It was observed with a switching angle of 1.8° and yielded a coherence correction of 1.1.

References. — (1) N. Vandenberg 2001, private communication; (2) Beasley et al. 2002.